ADVANCED FUNCTIONAL MATERIALS
www.afm-journal.de

Materials Views
www.MaterialsViews.com

Fe_3O_4 Nanoparticles Confined in Mesocellular Carbon Foam for High Performance Anode Materials for Lithium-Ion Batteries

Eunae Kang, Yoon Seok Jung, Andrew S. Cavanagh, Gi-Heon Kim, Steven M. George, Anne C. Dillon, Jin Kon Kim, and Jinwoo Lee**

Fe_3O_4 nanocrystals confined in mesocellular carbon foam (MSU-F-C) are synthesized by a "host–guest" approach and tested as an anode material for lithium-ion batteries (LIBs). Briefly, an iron oxide precursor, $Fe(NO_3)_3{\cdot}9H_2O$, is impregnated in MSU-F-C having uniform cellular pores ~30 nm in diameter, followed by heat-treatment at 400 °C for 4 h under Ar. Magnetite Fe_3O_4 nanocrystals with sizes between 13–27 nm are then successfully fabricated inside the pores of the MSU-F-C, as confirmed by transmission electron microscopy (TEM), dark-field scanning transmission electron microscopy (STEM), energy dispersive X-ray spectroscopy (EDS), X-ray diffraction (XRD), and nitrogen sorption isotherms. The presence of the carbon most likely allows for reduction of some of the Fe^{3+} ions to Fe^{2+} ions via a carbothermoreduction process. A Fe_3O_4/MSU-F-C nanocomposite with 45 wt% Fe_3O_4 exhibited a first charge capacity of 1007 mA h g^{-1} (Li^+ extraction) at 0.1 A g^{-1} (~0.1 C rate) with 111% capacity retention at the 150th cycle, and retained 37% capacity at 7 A g^{-1} (~7 C rate). Because the three dimensionally interconnected open pores are larger than the average nanosized Fe_3O_4 particles, the large volume expansion of Fe_3O_4 upon Li-insertion is easily accommodated inside the pores, resulting in excellent electrochemical performance as a LIB anode. Furthermore, when an ultrathin Al_2O_3 layer (<4 Å) was deposited on the composite anode using atomic layer deposition (ALD), the durability, rate capability and undesirable side reactions are significantly improved.

1. Introduction

To develop Li-ion batteries (LIBs) for next generation electric vehicles such as plug-in hybrid electric vehicles (PHEVs) and electric vehicles (EVs), many critical issues such as low cost, high energy/power density, durability, and safety must be addressed.[1] Nanostructured materials including nanoparticles, nanowires, and carbon nanotubes have been demonstrated for high energy/power density with significantly improved durability.[2] Metal oxides that undergo conversion- or displacement-type reactions ($MO_x + xLi^+ + xe^- \rightarrow M + xLi_2O$) are promising candidates for next generation anode materials because of their high theoretical capacity (~500–1000 mA h g^{-1}) compared with commercialized graphite (~372 mA h g^{-1}).[3] Iron oxides have multiple phases including hematite (α-Fe_2O_3, 1007 mA h g^{-1}) and magnetite (Fe_3O_4, 926 mA h g^{-1}) and have been extensively studied due to the low cost of iron.[4] However, the severe volume change of transition metal oxides that occurs upon Li^+ insertion and extraction causes mechanical degradation, resulting in rapid capacity loss especially at high charge–discharge rates.[5] Moreover, the low conductivity of transition metal oxides often further hastens the degradation process.

To improve the durability and high rate capability of transition metal oxides, various types of nano-architectures have been employed as anode materials for LIBs.[2a,2e,4] In order to mitigate the large-volume change

E. Kang, Prof. Dr. J. K. Kim, Prof. Dr. J. Lee
Department of Chemical Engineering
Pohang University of Science and Technology
San 31, Hyo-ja dong, Pohang, 790-784, Korea
E-mail: jkkim@postech.ac.kr; jinwoo03@postech.ac.kr
Prof. Dr. J. Lee
School of Environmental Science and Engineering
Pohang University of Science and Technology
San 31, Hyo-ja dong, Pohang, 790-784, Korea
Dr. Y. S. Jung, Dr. G.-H. Kim, Dr. A. C. Dillon
National Renewable Energy Laboratory
Golden, CO80401, USA
Mr. A. S. Cavanagh
Department of Physics
University of Colorado at Boulder
Boulder, CO 80309-0215, USA
Prof. Dr. S. M. George
George, Department of Chemistry and Biochemistry
and Department of Chemical and Biological Engineering
University of Colorado at Boulder
CO 80309-0215, USA

DOI: 10.1002/adfm.201002576

problem of transition metal oxides and increase the electronic conductivity, carbon coatings have been extensively explored.[2b,6] For example, carbon coated iron oxide nanoparticles were fabricated by heating carbon precursors including glucose and furfuryl alcohol in an inert atmosphere at 600 °C.[4c,4h] Wan et al. synthesized hematite nanospindles and carbon was coated on the surfaces to prevent agglomeration and enhance electronic conductivity.[4c] Hyeon et al. prepared magnetite/carbon nanocomposites by heating furfuryl alcohol and FeOOH nanoparticles synthesized by the hydrolysis of aqueous iron chloride solution. The resulting composites showed enhanced cycling performance by providing a physical barrier that prevented agglomeration and also enabled improved electronic conductivity.[4h]

However, the carbon coatings applied, thus far, on nanoparticles have the following drawbacks: i) Compact carbon coatings cannot allow residual buffer space to relieve stress arising from the large volume change (~93% for Fe_3O_4) during Li^+ insertion/extraction.[4g,6] ii) Transition metal oxides are generally reduced at high carbonization temperature.[7] In the iron oxide/carbon nanocomposites, the carbon source should be carbonized at 600 °C to prevent reduction of iron oxide to iron (or iron carbide).[4c,4h] In the later case, the carbon has very low electrical conductivity.[8] To obtain sufficient electrical conductivity, the carbon source generally should be heat-treated above 700 °C. The electrical conductivity of poly(furfuryl alcohol) derived carbon is increased by 4 orders of magnitude when the carbonization temperature is increased from 600 °C to 700 °C.[8]

Thus, it remains necessary to develop an approach for the fabrication of networks to accommodate volume expansion upon Li^+ insertion as well as enable high electronic conductivity.[2b] This may be achieved by a "host–guest" approach[9] that employs host materials with both large pore volumes and high electronic conductivity. The tailored pores then act as a buffer space for the volume expansion without a collapse of carbon host and simultaneously improve electronic conductivity. After the initial synthesis of ordered mesoporous carbons (OMCs) using mesoporous silica as hard templates, OMCs have been popularly adopted as electrode materials for fuel cells, supercapacitors, and batteries due to the interconnected and well-defined pore structure, with a large surface area.[10] OMCs are especially good candidates as host materials for LIBs. Ordered mesoporous carbon, CMK-3, has been previously employed to prepare electrochemically active carbon composites.[11] However, after loading electrochemically active nanomaterials, it may be difficult for the electrolyte to access the active materials inside the pores due to the single dimensions and small pore sizes (~3–4 nm) of the CMK-3. In order to accommodate a large quantity of electrochemically active materials and also enable facile penetration of the electrolyte into the pores, it is necessary to develop mesoporous carbons with larger pore sizes and volumes. Hyeon and coworkers synthesized mesocellular carbon foams, denoted as MSU-F-C that have a large pore size (>20 nm) and large pore volume (>1.8 $cm^3\ g^{-1}$) through controlled polymerization in a mesocellular silica foam template.[12] The pores of MSU-F-C are open in all directions due to the inherently isotropic pore structure. Thus the penetration of electrolyte is significantly enhanced compared with the pores of the two dimensional hexagonal structure of CMK-3.[13]

It was also previously demonstrated that durability and improved rate performance of LIB electrodes can be significantly improved by ultrathin (<1 nm) conformal Al_2O_3 coatings applied with atomic layer deposition (ALD).[14] The reaction sequences of an ALD process to deposit one atomic layer of Al_2O_3 utilizing trimethylaluminum (TMA) and H_2O as precursors are shown below:[15]

$$AlOH* + Al(CH_3)_3 \rightarrow AlO - Al(CH_3)_2* + CH_4 \quad (1)$$

$$AlCH3* + H_2O \rightarrow Al - OH* + CH_4 \quad (2)$$

The vapor phase ALD precursors can access the tortuous porous network being conformally deposited on any exposed surface. It has been demonstrated that ALD on as-fabricated composite electrodes enables maintaining electrical conductivity and serves not only as a protective layer for undesirable side reactions but also as a "glue" that maintains structural integrity during charge-discharge.[14] When using mesoporous electrode materials, the ALD coating can be deposited conformally on all of the inner wall surfaces.

Herein, we report on the fabrication of tailored Fe_3O_4-MSU-F-C nanocomposites using the host–guest approach. The resulting composites show high capacities of ~800–1000 mA h g^{-1} at 0.1 A g^{-1} (~0.1 C rate), durable cycling performance, and high rate capability. Furthermore, when a ultrathin Al_2O_3 layer (<4 Å) is deposited on the composite anode by using atomic layer deposition (ALD), the durability and rate capability is greatly enhanced.

2. Results and Discussion

2.1. Synthesis of Fe_3O_4/MSU-F-C

The fabrication process for Fe_3O_4/MSU-F-C composites is depicted in **Scheme 1**. MSU-F-C with large interconnected

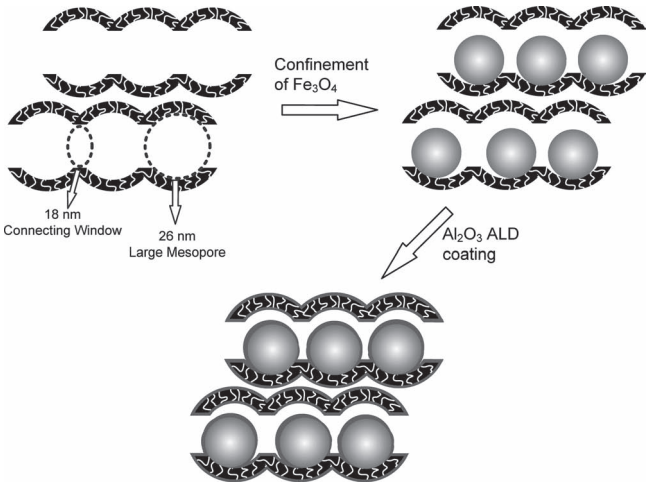

Scheme 1. Schematic representation of the preparation of Fe_3O_4/MSU-F-C samples. After incorporating Fe_3O_4 nanocrystals inside the pores, to further improve long-term durability and rate-capability, the conformal ultrathin protective Al_2O_3 coating was deposited with ALD.

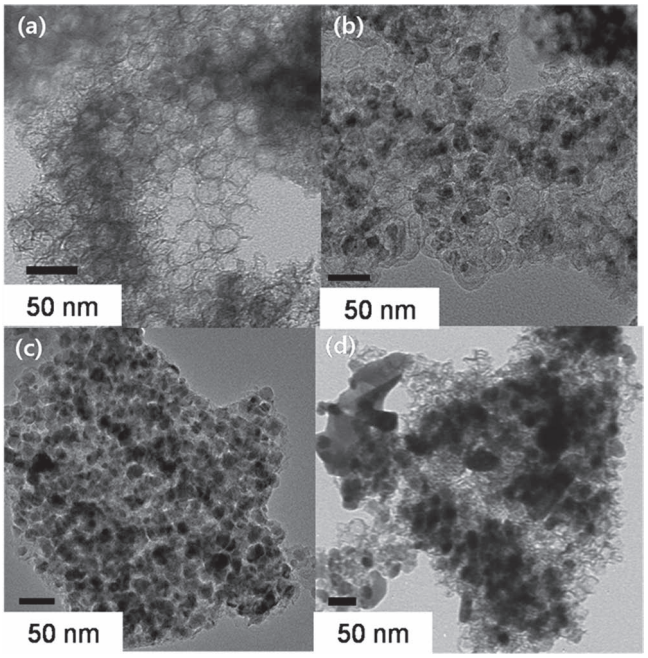

Figure 1. TEM images of a) MSU-F-C, b) Fe_3O_4/MSU-F-C-45, c) Fe_3O_4/MSU-F-C-61, and d) Fe_3O_4/MSU-F-C-71.

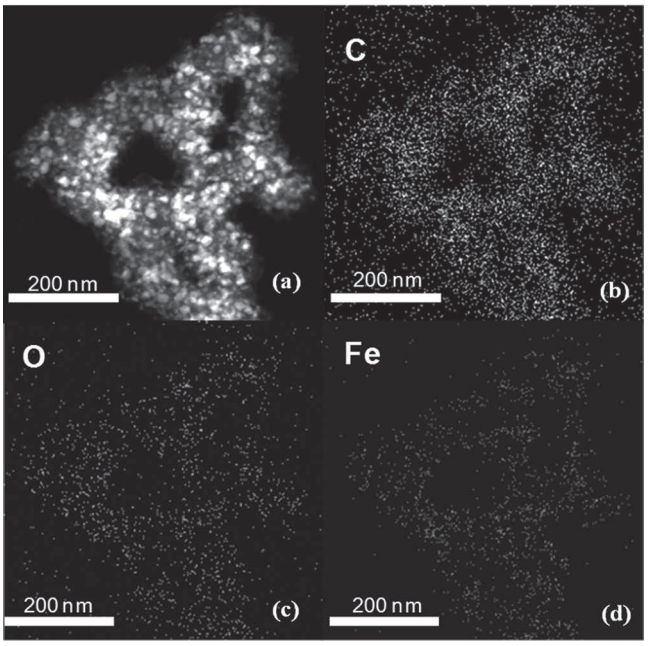

Figure 2. a) Dark-field STEM image of Fe_3O_4/MSU-F-C-45 and b–d) elemental mapping with EDS showing uniform distribution of Fe_3O_4 throughout MSU-F-C particles.

pores was first prepared by employing mesocellular silica as a hard template.[12a] As shown in the transmission electron microscopy (TEM) image (**Figure 1**a), MSU-F-C contains uniform cellular pores with diameters of ~30 nm as well as several hundred nanometer sized individual particles (Supporting Information, Figure S1). Different quantities of Fe_3O_4 were loaded inside the cellular pores of MSU-F-C by impregnation of $Fe(NO_3)_3 \cdot 9H_2O$ dissolved in ethanol, followed by heat-treatment in Ar at 400 °C. It is known that π-electrons of basal planes or oxygen containing groups (chromenes, ketones, and pyrones) present in carbons provide basic sites on the surface of carbons after heat-treatment at high temperature (above 700 °C).[16] The acid–base interaction between acidic salt $Fe(NO_3)_3 \cdot 9H_2O$ and basic sites on carbon surfaces most likely drives the facile infiltration of $Fe(NO_3)_3 \cdot 9H_2O$ inside the pores, leading to Fe_3O_4 nanocrystals confined in mesocellular pores in MSU-F-C. During conversion of $Fe(NO_3)_3 \cdot 9H_2O$ to Fe_3O_4, a reducing gas (such as Ar/H_2) was not needed for the partial reduction of Fe^{3+} ions. Under Ar atmosphere, part of the Fe^{3+} ions can be reduced to Fe^{2+} by the π-electrons of the basal planes present on the carbon surfaces as consistent with previous studies,[2g] where magnetite, Fe_3O_4, is formed.[17] The loading levels of Fe_3O_4 were controlled to be 45 wt%, 61 wt%, and 71 wt%, and the resulting Fe_3O_4/MSU-F-C nanocomposites were denoted as Fe_3O_4/MSU-F-C-*X* with *X* indicating loading level.

Al_2O_3 ALD was performed on as-prepared Fe_3O_4/MSU-F-C-61 composite electrodes. The vapor phase precursors for Al_2O_3 ALD, TMA and H_2O, can diffuse through the mesopores (18 nm) (Scheme 1) in order to deposit conformal single Al_2O_3 layers. The basal planes of carbonaceous materials have no reactive functional groups to initiate the ALD reactions. Only dangling bonds such as C–O–H on the edge site of the carbon will initiate the ALD reaction. Thus, in order to deposit conformal coatings on the inert basal plane of the carbon and thereby achieve maximum surface coverage, a TMA/NO_2 pretreatment was also performed prior to the TMA/H_2O ALD cycles.[14b]

TEM images of various Fe_3O_4/MSU-F-C samples are displayed in Figure 1. For Fe_3O_4/MSU-F-C-45, the size of Fe_3O_4 nanoparticles is much smaller than that of the cellular pores and the majority of the nanoparticles are located inside the pores. This structure is favorable for achieving high durability and high rate capability. The dark field scanning transmission electron microscopy (STEM) image of Fe_3O_4/MSU-F-C-45 (**Figure 2**a) confirms that Fe_3O_4 nanocrystals are embedded in the mesoporous carbon matrix. The elemental mapping of C, O, and Fe by energy dispersive X-ray spectroscopy (EDS) on Fe_3O_4/MSU-F-C-45 (Figure 2b, c, d) also shows that Fe_3O_4 nanoparticles are homogeneously distributed in the mesoporous carbon matrix.

The XRD patterns of the various samples are shown in **Figure 3**. All XRD patterns index well with those of magnetite (Fe_3O_4 – JCDPS No. 19-0629), indicating that some of the Fe^{3+} is reduced to Fe^{2+} during the Ar heat-treatment. The particle size of Fe_3O_4 in Fe_3O_4/MSU-F-C-45 calculated using Debye–Scherer equation[18] from the XRD patterns (Figure 3) is ~13.1 nm, in good agreement with the TEM data. When the amount of Fe_3O_4 in the composite materials was increased to 61 wt% (Fe_3O_4/MSU-F-C-61), the particle size estimated by the XRD pattern (Figure 3) is increased to ~20.1 nm. Although the particle size is increased, most of the Fe_3O_4 particles are still located inside the pores (Figure 1c). Further increasing the loading of Fe_3O_4 (Fe_3O_4/MSU-F-C-71) causes the formation of larger Fe_3O_4 particles (>100 nm) with some of the particles now outside the pores (Figure 1d) and a calculated size of ~27.0 nm.

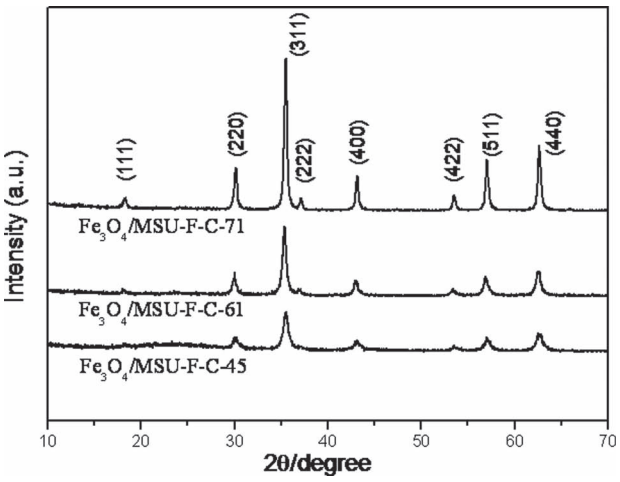

Figure 3. X-ray diffraction patterns of Fe_3O_4/MSU-F-C-45, Fe_3O_4/MSU-F-C-61, and Fe_3O_4/MSU-F-C-71. The peaks in the XRD patterns match well with the standard magnetite (Fe_3O_4) crystal structure (Fe_3O_4-JCDPS No. 19-0629).

The pore structure and physical properties of MSU-F-C and Fe_3O_4-loaded composites were characterized with nitrogen sorption studies (**Figure 4**). The N_2 adsorption/desorption isotherms of MSU-F-C exhibit hysteresis at ~0.7 P/P_0 and ~0.9 P/P_0. The increase at ~0.7 P/P_0 is attributed to the small macrospores generated by dissolution of the microcellular silica walls,[11a] and the hysterics loop at ~0.9 P/P_0 is attributed to the large uniform cellular macrospores. The incorporation of Fe_3O_4 nanocrystals leads to decreased amount of adsorbed N_2. The existence of large pores (25.9 nm) is also apparent in the pore size distribution calculated from the nitrogen isotherms using the BJH (Barrett–Joyner–Helena) method. From the desorption branch of N_2 isotherms, the size of small pores generated by dissolution of template silica walls is estimated to be 4.8 nm.[12a] Since most of Fe_3O_4 nanocrystals are larger than 10 nm, as observed in the TEM image (Figure 1), Fe_3O_4 nanocrystals are mainly present inside large cellular pores. As shown in **Table 1**, the BET surface area and single point total pore volume of bare MSU-F-C at $P/P_0 = 0.99$ are determined to be 854 $m^2\ g^{-1}$ and 1.80 $cm^3\ g^{-1}$, respectively. After incorporation of Fe_3O_4 in the pores of MSU-F-C, the surface area and pore volume are, not surprisingly, significantly decreased (Table 1). Because the Fe_3O_4 nanoparticles are primarily incorporated into the main pores of MSU-F-C,

Table 1. Textural properties of MSU-F-C and Fe_3O_4 nanocrystal/MSU-F-C composite samples.

Sample Name	Pore volume [$cm^3\ g^{-1}$][a)]	BET surface area [$m^2\ g^{-1}$]
MSU-F-C	1.80	832
Fe_3O_4/MSU-F-C-45	0.61	446
Fe_3O_4/MSU-F-C-61	0.25	222
Fe_3O_4/MSU-F-C-71	0.19	154

[a)] Pore volume was measured at $P/P_0 = 0.99$.

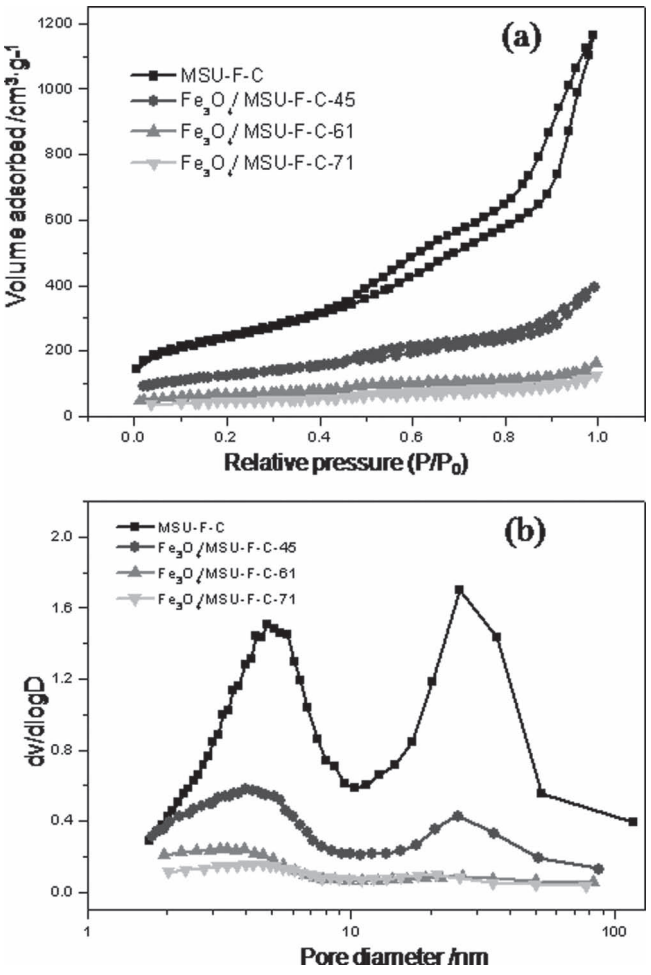

Figure 4. a) Nitrogen adsorption–desorption isotherms of samples and b) corresponding pore size distributions obtained using BJH method from the adsorption branch of the N_2 adsorption isotherm.

the pore volume of the large pores are decreased much more dramatically than the small pores. In the case of Fe_3O_4/MSU-F-C-61 and Fe_3O_4/MSU-F-C-71, the population of large cellular pores is significantly reduced, indicating that most of the large cellular pores are occupied by Fe_3O_4 nanocrystals.

To show that the Al_2O_3 layer is uniformly coated on the surface of Fe_3O_4 nanoparticles and MSU-F-C pores, we performed energy dispersive X-ray spectroscopy (EDS) elemental mapping on the Fe_3O_4/MSU-F-C-61 powders coated with 2 Al_2O_3 ALD cycles with TMA/NO_2 pretreatment during imaging with TEM. The sample was sectioned at 100 nm thickness with a microtoming machine. As shown in **Figure 5**a, most of the Fe_3O_4 nanoparticles are located inside the cellular pores of MSU-F-C. EDS mapping of C and Fe (Figure 5b and c) provides further evidence that Fe_3O_4 nanoparticles are surrounded by hollow carbon materials. As we expected, EDS mapping of Al (Figure 5d) clearly shows that aluminum atoms are distributed between hollow carbon materials and Fe_3O_4 nanoparticles. With the TEM and EDS elemental mapping characterization, we confirm that thin Al_2O_3 ALD layer is uniformly coated on the surface of Fe_3O_4 nanoparticles and MSU-F-C pores.

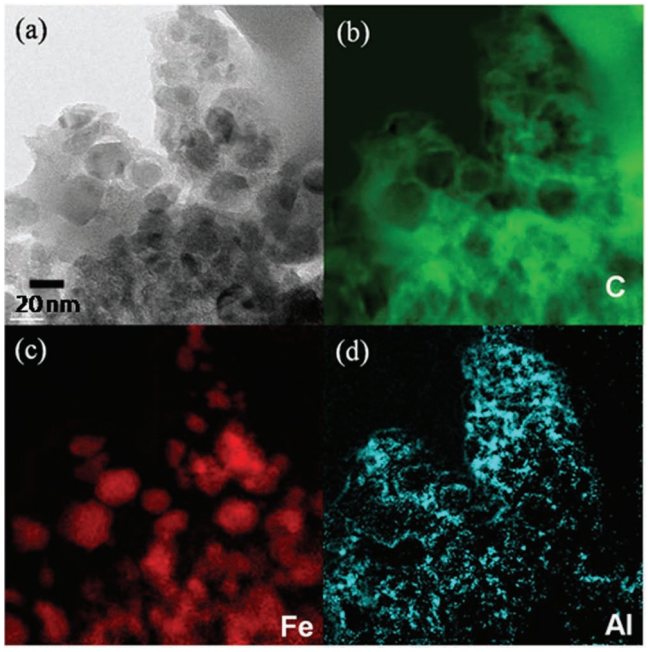

Figure 5. a) Cross-sectional TEM image of Fe_3O_4/MSU-F-C-61 powders coated with 2 Al_2O_3 ALD cycles with TMA/NO_2 pretreatment obtained by ultra-thin microtoming methods (sectioned at 100 nm thickness). b) C, c) Fe, and d) Al EDS mapping corresponding to a TEM image shown in (a).

2.2. Electrochemical Characteristics of Fe_3O_4/MSU-F-C

As some of the Fe_3O_4 particles in the Fe_3O_4/MSU-F-C-71 composite exist outside the mesoporous carbon pores, we performed electrochemical characterization for Fe_3O_4/MSU-F-C-45 and Fe_3O_4/MSU-F-C-61. **Figure 6** represents the first and second discharge–charge voltage profiles at 0.1 A g^{-1} at room temperature. **Table 2** summarizes the electrochemical performances. As seen in Table 2 and Figure 6a, Fe_3O_4/MSU-F-Cs exhibit significant first discharge (Li^+ insertion) capacities (Fe_3O_4/MSU-F-C-45: 1710 mA h g^{-1}, Fe_3O_4/MSU-F-C-61: 1357 mA h g^{-1}), indicating severe side reactions related to electrolyte decomposition at the surface. The first charge capacities of Fe_3O_4/MSU-F-C-45 and Fe_3O_4/MSU-F-C-61 also exceed the theoretical limit of even pure Fe_3O_4 (926 mA h g^{-1}). This indicates that a significantly large capacity may be attributed to MSU-F-C, which is confirmed by the extremely high capacity of MSU-F-C (charge: 983 mA h g^{-1}) (Table 2 and Figure S2). Although even smaller loading of Fe_3O_4 (Fe_3O_4/MSU-F-C-45) leads to higher capacity than Fe_3O_4/MSU-F-C-61, the first cycle coulombic efficiency (Table 2) is lower. This is a disadvantage because it indicates more loss of Li^+ from the cathode material in a practical full cell configuration will occur. Lower density of Fe_3O_4/MSU-F-C with lower loading of Fe_3O_4 also leads to lower volumetric capacity. First discharge (Li^+ insertion) curves of Fe_3O_4/MSU-F-Cs in Figure 6a exhibit a short sloping region above ~1 V (Region I)

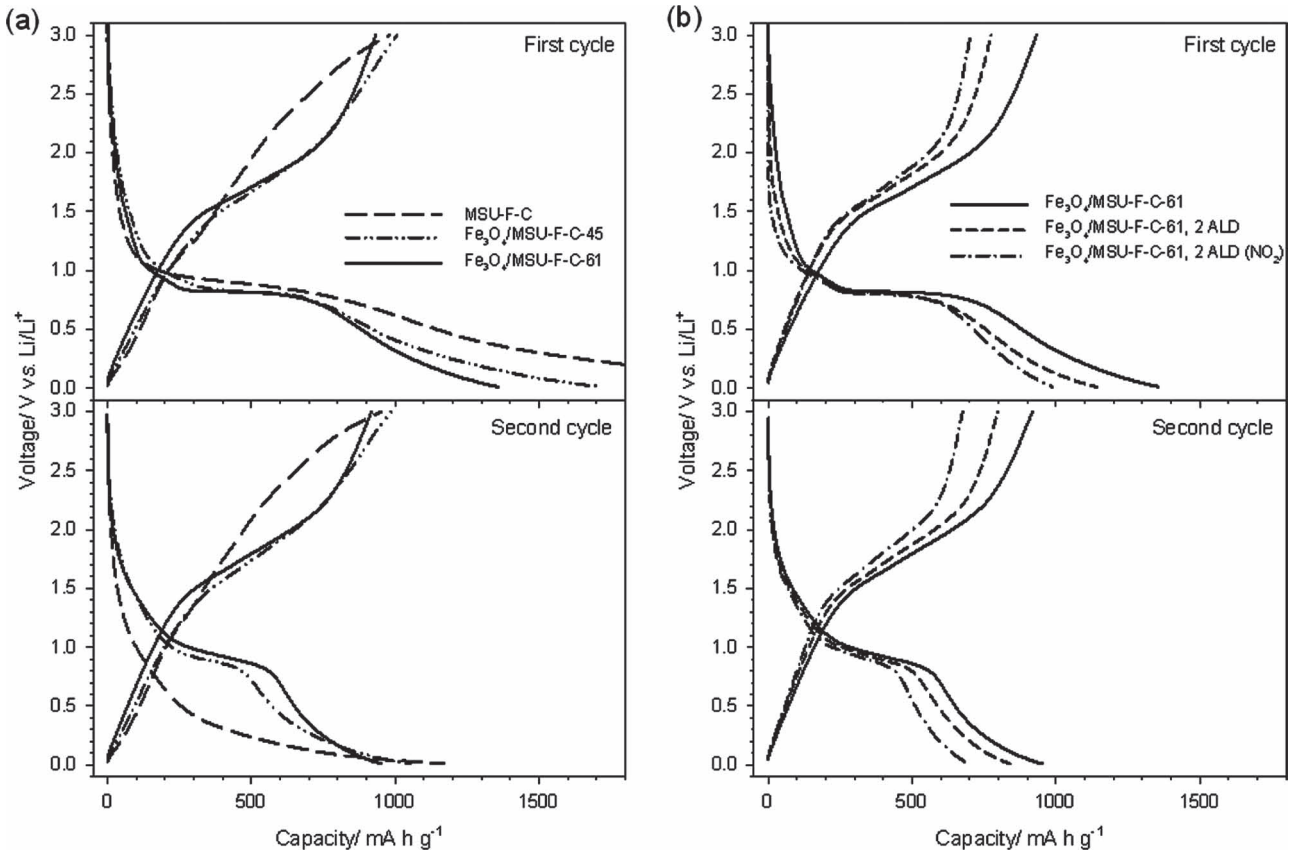

Figure 6. First and second discharge-charge curves at 0.1 A g^{-1} for a) bare Fe_3O_4/MSU-F-C with 45 wt% and 61 wt% of Fe_3O_4. For reference, the curves of MSU-F-C are also shown and b) Al_2O_3-coated MSU-F-C-61 with 2 cycles of ALD with and without TMA/NO_2 pretreatment.

Table 2. Electrochemical performance of the electrodes.

Sample Name	Capacity at 1st cycle [mA h g^{-1}]		CE [%][a]	Current [mA g^{-1}]	Capacity retention [%][b]		
	Discharge	Charge			50th	100th	150th
MSU-F-C	2818	983	34	2	80	70	67
Micro-Fe_3O_4	1039	768	74	0.5	65	42	
Nano-Fe_3O_4/MSU-F-C mixture (61 wt%)	2396	1190	50	2	20		
Fe_3O_4/MSU-F-C-61	1357	932	69	0.5	98	78	56
				2	67	32	20
Fe_3O_4/MSU-F-C-45	1710	1007	59	0.5	108	114	111
				2	86	80	74
Fe_3O_4/MSU-F-C-61, 2 ALD	1141	775	68	0.5	100	87	73
				2	72	49	24
Fe_3O_4/MSU-F-C-61, 2 ALD (NO_2)	987	703	71	0.5	92	81	
				2	89	73	47

[a]Couloumbic efficiency at 1st cycle. [b] Capacity retention of the charge capacity at given cycle with respect to that at the 3rd cycle.

and a subsequent plateau at ~0.8 V (Region II), followed by long sloping region down to 0 V (Region III). The plateau in region II is primarily attributed to the conversion reaction of Fe_3O_4 with Li^+ ($Fe_3O_4 + 8Li^+ + 8e^- \rightarrow 4Li_2O$), which explains the increased capacity in region II where the fraction of Fe_3O_4 is increased from 45 wt% to 61 wt%. In contrast, the capacity in region I and III decreases by increasing the amount of Fe_3O_4. This implies that the capacities in region I and III are related to side reactions due to the high surface area.

The voltage profiles of Fe_3O_4/MSU-F-C-61 after two cycles of Al_2O_3 ALD coating with and without TMA/NO_2 pretreatment are shown in Figure 6b. The Al_2O_3 ALD coatings with and without TMA/NO_2 pretreatment result in lower capacities. There are two possible explanations for this decrease in capacity: i) Due to the extremely high surface area of Fe_3O_4/MSU-F-C-61, the weight fraction of even the very thin Al_2O_3 coating (~4 Å) may be significant. This may lead to an overestimated mass of active material (Fe_3O_4 and carbon). ii) The extremely high capacities of Fe_3O_4/MSU-F-C arise partly from abnormal reversible Li^+ storage on the surface sites of Fe_3O_4 and/or MSU-F-C.[19] Due to the excellent conformallity of the Al_2O_3 coating by ALD, this surface reactive site can be inactivated by the thin Al_2O_3 coating, resulting in significantly decreased capacities in region I and III in the first and second discharge (Figure 6b) and correspondingly decreased intensity of differential capacity at first and second discharge ('#' and '^' in Figure S3b). Comparing the ALD coated Fe_3O_4/MSU-F-C-61 with and without TMA/NO_2 pretreatment, the TMA/NO_2 pretreated samples exhibit reduced capacities in region I and III, implying significantly reduced surface reactions related to the carbon host, MSU-F-C.

The durability of Fe_3O_4/MSU-F-Cs was assessed by cycling in the range of 0.01–3.00 V (*vs.* Li/Li^+) at 0.1 A g^{-1} for the first two cycles and at 0.5 A g^{-1} (**Figure 7**a) and 2 A g^{-1} (Figure 7b) for the subsequent cycles. As displayed in Figure 7a, comparing micro-Fe_3O_4 (<5 μm, hexagon) with Fe_3O_4/MSU-F-Cs (rectangle and diamond) reveals significantly improved performance, clearly showing that the nano-architecture of Fe_3O_4/MSU-F-C mitigates volume change stress. However, an electrode made of Fe_3O_4 nanoparticles without carbon nanocomposite structure results in fast capacity fading. Electrode fabricated by mechanical mixing Fe_3O_4 nanoparticles (~13 nm) with MSU-F-C (Fe_3O_4:MSU-F-C = 61:39 weight ratio) is displayed in Figure 7. The Fe_3O_4 nanoparticles were synthesized via base-catalyzed precipitation method.[20] The detailed characterization is displayed in the Supporting Information (Figure S4). The mixture electrode exhibits much poorer performance than the Fe_3O_4/MSU-F-C-61. This observation is in line with the previous reports where the mixture electrode comprised of Sn and carbon nanoparticles showed much poorer performances than Sn-carbon core-shell structured particles.[2b,6a] In the simple mixture electrode, the electrical contact between Fe_3O_4 nanoparticles and carbon may be loosened during the repeated volume change of Fe_3O_4. In contrast, the intimate contact between Fe_3O_4 nanoparticles and mesoporous carbon (MSU-F-C) can be well maintained without a collapse of carbon host for the nanocomposite structure (Fe_3O_4/MSU-F-Cs). Also, uneven distribution of the Fe_3O_4 nanoparticles in the mixture electrode may cause more severe mechanical disintegration problem than the Fe_3O_4/MSU-F-C nanocomposite electrode. By increasing the amount of Fe_3O_4 from 45 wt% to 61 wt%, the performance decreases. The increased occupied volume of Fe_3O_4 inside the pores can lead to decreased buffer space for volume expansion of Fe_3O_4 during Li^+ insertion. Although the Al_2O_3 coating with two cycles of ALD with and without TMA/NO_2 pretreatment on Fe_3O_4/MSU-F-C-61 leads to decreased capacities, two cycles of ALD slightly improves the cycling durability. It was suggested that Al_2O_3 ALD can act not only as a protective layer to mitigate undesirable surface reactions which can degrade the performance[14a,14b,14d] but also as a "glue" to enhance the structural integrity.[14c] As shown by the increased coulombic efficiency for the ALD samples with TMA/NO_2 pretreatment (Table 2), the Al_2O_3 ALD can enhance the stability of the electrode–electrolyte interface. When the current density is

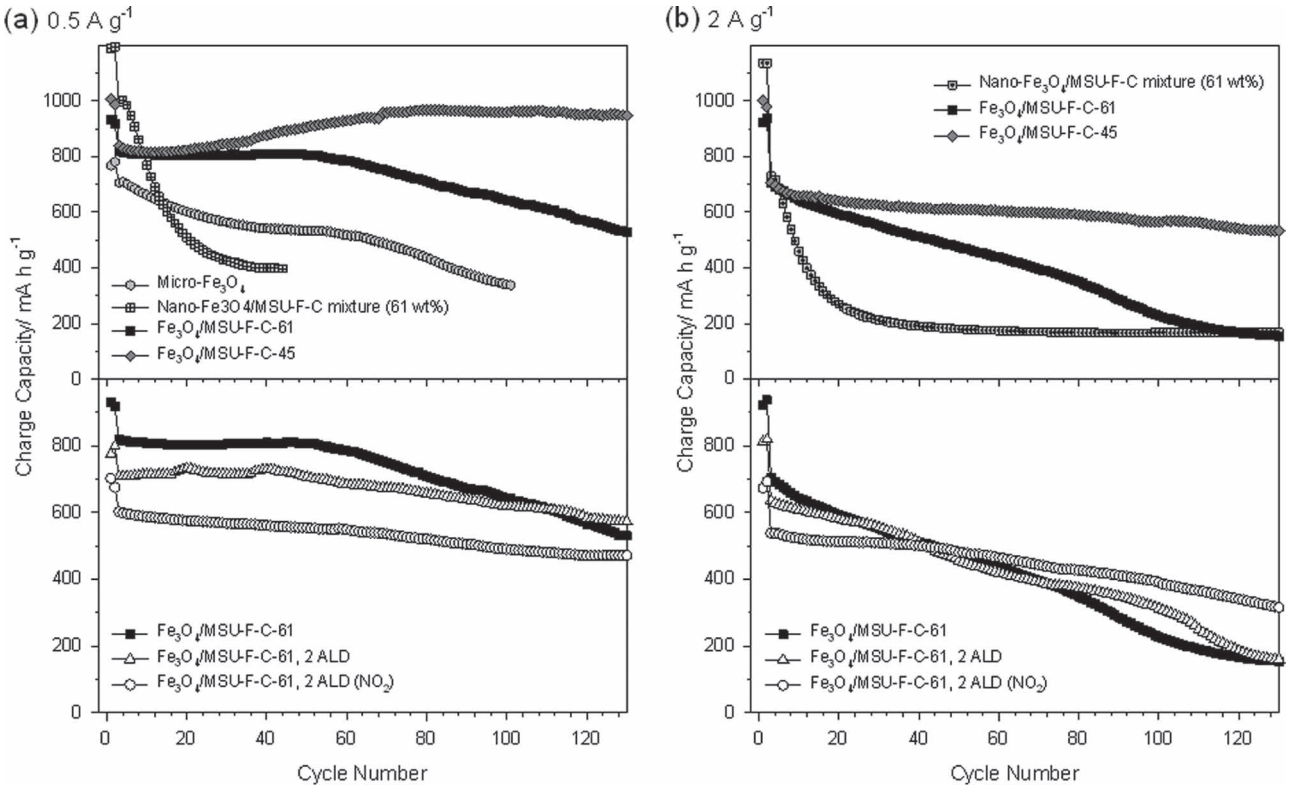

Figure 7. Cycling performance of Fe_3O_4/MSU-F-Cs and ALD coated Fe_3O_4/MSU-F-Cs, a) at 0.5 A g^{-1} and b) at 2 A g^{-1}.

increased, the difference in the cycling performance is magnified because rapid structural changes of Fe_3O_4 will cause more severe stress on the structural integrity, and any polarization will be increased. At high current (2 A g^{-1}), as seen in Figure 7b, the capacity of bare Fe_3O_4/MSU-F-C-61 decays rapidly. In contrast, two cycles of Al_2O_3 with TMA/NO_2 pretreatment significantly enhances performance.

An additional advantage of the Fe_3O_4/MSU-F-C composite is the enhancement of rate capability due to the short Li^+ diffusion path and easy access of the electrolyte through large interconnected three dimensional pores as well as good electrical connectivity. The charge capacity as a function of current density is displayed in **Figure 8**. Compared with micro-Fe_3O_4 which are <5 μm in particle size (open circle), Fe_3O_4/MSU-F-Cs exhibits excellent rate performance. Compared with Fe_3O_4/MSU-F-C-45, higher Fe_3O_4 loading (61 wt%) results in poorer rate performance, which can be attributed to the lower pore volume than that occurring for the 45 wt% Fe_3O_4 loading. Furthermore, two cycles of Al_2O_3 ALD improves the rate performance of Fe_3O_4/MSU-F-C-61. The Al_2O_3 ALD may form a better electrolyte–electrode interface and transfer Li^+ faster than the native solid electrolyte interphase (SEI) which often limits the kinetic properties.[14] Additionally, the improved rate performance by ALD may come from well-maintained electronic conductivity during the volume change of Fe_3O_4.[14c] However, the very conformal coating by ALD with TMA/NO_2 pretreatment results in poorer rate performance than bare samples because of the Li^+ insulating property of Al_2O_3.[14a,14b]

3. Conclusions

Fe_3O_4 nanoparticles confined in mesocellular carbon foam were successfully synthesized by impregnating an Fe precursor in a mesoporous carbon host. We have also demonstrated that this Fe_3O_4/MSU-F-C nanostructure can not only mitigate durability issues caused by the large-volume change of Fe_3O_4 during Li^+ insertion/extraction but also lead to excellent rate performance.

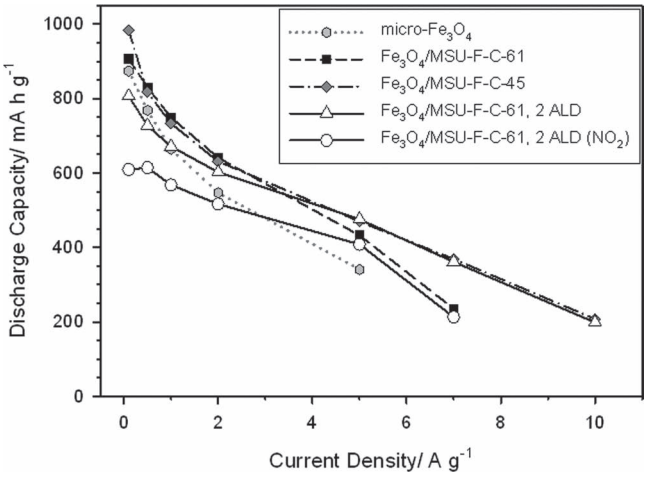

Figure 8. Rate capability of micro-Fe_3O_4 and Fe_3O_4/MSU-F-Cs and ALD coated Fe_3O_4/MSU-F-Cs.

The combined effect of nanosized Fe_3O_4, extra pore volume to accommodate volume expansion of Fe_3O_4, and large three dimensional interconnected mesoporous carbon pores with excellent electronic connectivity account for the excellent performance. Additionally, ALD of Al_2O_3 has been shown to mitigate undesirable surface side reactions of these high-surface area materials.

4. Experimental Section

Synthesis of Fe_3O_4/MSU-F-C: Mesocellular carbon foam, MSU-F-C, was synthesized according to previous reports.[12a] Aluminated MSU-F silica (Si/Al = 20) was wetted with furfuryl alcohol, and the composite was heat-treated at 80 °C under static vacuum for 12 h for the polymerization of furfuryl alcohol. The resulting composite was carbonized at 850 °C for 2 h under a nitrogen atmosphere and etched by HF solution (5 wt%) to produce MSU-F-C. To prepare Fe_3O_4-MSU-F-C, the desired amount of $Fe(NO_3)_3{\cdot}9H_2O$ was dissolved in ethanol (20 mL), and then MSU-F-C (1g) was slowly added with stirring. After evaporation of ethanol at room temperature while stirring, the resulting material was heated to 400 °C for 4 h under flowing Ar to get Fe_3O_4/MSU-F-C. As a counter reference sample, micrometer-sized Fe_3O_4 powders (<5 μm, Aldrich) were tested.

Al_2O_3 ALD on Fe_3O_4/MSU-F-C: Al_2O_3 ALD films were grown directly on Fe_3O_4-MSU-F-C electrodes. For the elemental mapping by EDS, the Al_2O_3 ALD films were also grown on Fe_3O_4-MSU-F-C powders using a rotary ALD reactor.[14] For the Al_2O_3 ALD, TMA (97%) and HPLC (high performance liquid chromatography) grade H_2O was obtained from Sigma-Aldrich. For the TMA/NO_2 nucleation treatment, commercial purity grade NO_2 (99.5%) was acquired from Airgas. The typical growth rate for the chemistry is 1.1 Å per cycle[21]. Also detailed ALD reaction sequences were described in previous reports[14].

Electrochemical characterization: The Fe_3O_4/MSU-F-C composite electrode was prepared by spreading Fe_3O_4/MSU-F-C powders, carbon black (super C65, TIMCAL Ltd.), and PVDF (polyvinylidene fluoride, binder) (8:1:1 weight ratio) on a piece of Cu foil. 2032-type coin cells of two-electrodes (Fe_3O_4/MSU-F-C)/Li were assembled in an Ar-filled dry box. $LiPF_6$ (1.0 M) in a mixture of ethylene carbonate (EC) and diethyl carbonate (DEC) (1:1 volume ratio) was used as the electrolyte. As a separator, a porous 25 μm thick polypropylene (PP)/polyethylene/PP trilayer film (2325, Celgard) was used. The galvanostatic charge–discharge cycling was performed between 0.01–3.00 V at 0.1 A g^{-1} for the first two cycles and 0.5 A g^{-1} or 2 A g^{-1} for the subsequent cycles at room temperature. To test rate performance, the electrodes were first cycled at 0.1 A g^{-1} for 5 cycles, and the current was increased in stages to 0.5 A g^{-1}, 1 A g^{-1}, 2 A g^{-1}, 5 A g^{-1}, 7 A g^{-1}, and 10 A g^{-1}. The capacity as a function of current density plotted in the Figure 7 was chosen from that of the second cycle of each stage.

Supporting Information

Supporting Information is available from the Wiley Online Library or from the author.

Acknowledgements

E.K. and Y.S.J. contributed equally to experimental and scientific development. This research was supported by the National Research Foundation of Korea Grant funded by the Korean Government (2009-0064640, 2009-0084771) and by the U.S. Department of Energy under Contract No. DE-AC36-08-GO28308 through: the NREL Laboratory Directed Research and Development Program with the National Renewable Energy Laboratory.

Received: December 7, 2010
Revised: February 28, 2011
Published online: April 26, 2011

[1] Idaho National Laboratory website, Battery Test Manual for Plug-In Hybrid Electric Vehicle, http://www.inl.gov (accessed April 2011).
[2] a) A. S.Aricò, P. Bruce, B. Scrosati, J.-M. Tarascon, W. Van Schalkwijk, *Nat. Mater.* **2005**, *4*, 366; b) K. T. Lee, Y. S. Jung, S. M. Oh, *J. Am. Chem. Soc.* **2003**, *125*, 5652; c) M. S. Park, S. A. Needham, G.-X. Wang, Y. M. Kang, J. S. Park, S. X. Dou, H. K. Liu, *Chem. Mater.* **2007**, *19*, 2406; d) S. Lim, C. S. Yoon, J. Cho, *Chem. Mater.* **2008**, *20*, 4560; e) S.-H. Lee, Y.-H. Kim, R. Deshpande, P. A. Parilla, E. Whitney, D. T. Gillaspie, K. M. Jones, A. H. Mahan, S. Zhang, A. C. Dillon, *Adv. Mater.* **2008**, *20*, 3627; f) E. Hosono, T. Kudo, I. Honma, H. Matsuda, H. Zhou, *Nano. Lett.* **2009**, *9*, 1045; g) C. Ban, Z. Wu, D. T. Gillespie, L. Chen, Y. Yan, J. L. Blackburn, A. C. Dillon, *Adv. Mater.* **2010**, *22*, E145.
[3] a) P. Poizot, S. Laruelle, S. Grugeon, L. Dupont, J.-M. Tarascon, *Nature* **2000**, *407*, 496; b) P. Poizot, S. Laruelle, S. Grugeon, J.-M. Tarascon, *J. Electrochem. Soc.* **2002**, *149*, A1212; c) D. Larcher, D. Bonnin, R. Cortes, I. Rivals, L. Personnaz, J.-M. Tarascon, *J. Electrochem. Soc.* **2003**, *150*, A1643; d) J. Chen, L. Xu, W. Li, X. Gou, *Adv. Mater.* **2005**, *17*, 582; e) K. M. Shaju, F. Jia, A. Debart, P. G. Bruce, *Phys. Chem. Chem. Phys.* **2007**, *9*, 1837.
[4] a) M. V. Reddy, T. Yu, C.-H. Sow, Z. X. Shen, C. T. Lim, G. V. S. Rao, B. V. R. Chowdari, *Adv. Funct. Mater.* **2007**, *17*, 2792; b) Z. Wu, K. Yu, S. Zhang, Y. Xie, *J. Phys. Chem. C.* **2008**, *112*, 11307; c) W.-M. Zhang, X.-L. Wu, J.-S. Hu, Y.-G. Guo, L.-J. Wan, *Adv. Funct. Mater.* **2008**, *18*, 3941; d) L. Wang, Y. Yu, P. C. Chen, D. W. Wang, C. H. Chen, *J. Power Sources* **2008**, *183*, 717; e) H. Liu, G. Wang, J. Wang, D. Wexler, *Electrochem. Commun.* **2008**, *10*, 1879; f) T. Muraliganth, A. V. Murugan, A. Manthiram, *Chem. Commun.* **2009**, 7360; g) G. H. Lee, J. G. Park, Y. -M. Sung, K. Y. Chung, W. I. Cho, D.-W. Kim, *Nanotechnology.* **2009**, *20*, 295205; h) Y. Piao, H. S. Kim, Y.-E. Sung, T. Hyeon, *Chem. Commun.* **2010**, *46*, 118; i) J. Liu, T. Li, H. Fan, Z. Zhu, J. Jiang, R. Ding, Y. Hu, X. Huang, *Chem. Mater.* **2010**, *22*, 212.
[5] a) J. Li, H. M. Dahn, L. J. Krause, D.-B. Le, J. R. Dahn, *J. Electrochem. Soc.* **2008**, *155*, A812; b) Y. S. Jung, S. Lee, D. Ahn, A. C. Dillon, S.-H. Lee, *J. Power Sources* **2009**, *188*, 286; c) J. Kim, M. K. Chung, B. H. Ka, J. H. Ku, S. Park, J. Ryu, S. M. Oh, *J. Electrochem. Soc.* **2010**, *157*, A412.
[6] a) Y. S. Jung, K. T. Lee, J. H. Ryu, D. Im, S. M. Oh, *J. Electrochem. Soc.* **2005**, *152*, A1452. b) Y. S. J ung, K. T. Lee, *Electrochim. Acta* **2007**, *52*, 7061.
[7] a) J. Lee, D. Lee, E. Oh, J. Kim, Y.-P. Kim, S. Jin, H.-S. Kim, Y. Hwang, J. H. Kwak, J.-G. Park, C.-H. Shin, J. Kim, T. Hyeon, *Angew. Chem.Int. Ed.* **2005**, *44*, 7427; b) J. Lee, S. Jin, Y. Hwang, J.-G. Park, H. M. Park, T. Hyeon, *Carbon.* **2005**, *43*, 2536.
[8] J.-I. Ozaki, M. Mitsui, Y. Nishiyama, J. D. Cashion, L. J. Brown, *Chem. Mater.* **1998**, *10*, 3386.
[9] Y. Wan, H. Yang, D. Zhao, *Acc. Chem. Res.* **2006**, *39*, 423.
[10] a) J. Lee, S. Yoon, T. Hyeon, S. M. Oh, K. B. Kim, *Chem. Commun.* **1999**, 2177; b) J. Lee, S. Yoon, S. M. Oh, C.-H. Shin, T. Hyeon, *Adv. Mater.* **2000**, *12*, 359; c) S. H. Joo, S. J. Choi, I. Oh, J. Kwak, Z. Liu, O. Terasaki, R. Ryoo, *Nature* **2001**, *412*, 169; d) C. Yu, J. Fan, B. Tian, D. Zhao, G. D. Stucky, *Adv. Mater.* **2002**, *14*, 1742; e) H. Zhou, S. Zhu, M. Hibino, I. Honma, M. Ichihara, *Adv. Mater.* **2003**, *15*, 2107; f) S. Zhu, H. Zhou, M. Hibino, I. Honma, M. Ichihara, *Adv. Funct. Mater.* **2005**, *15*, 381; g) Y. Xia, R. Mokaya, *Adv. Mater.* **2004**, *16*, 1553;

h) C. H. Kim, D.-K. Lee, T. J. Pinnavaia, *Langmuir* **2004**, *20*, 5137; i) J. Lee, J. Kim, T. Hyeon, *Adv. Mater.* **2006**, *18*, 2073.
[11] a) S. Zhu, H. Zhou, M. Hibino, I. Honma, M. Ichihara, *Adv. Funct. Mater.* **2005**, *15*, 381; b) Z. Ji, K. T. Lee, L. F. Nazar, *Nat. Mater.* **2009**, *8*, 500.
[12] a) J. Lee, K. Sohn, T. Hyeon, *J. Am. Chem. Soc.* **2001**, *123*, 5146; b) J. Lee, K. Sohn, T. Hyeon, *Chem. Commun.* **2002**, 2674.
[13] S. Jun, S. H. Joo, R. Ryoo, M. Kruk, M. Jaroniec, Z. Liu, T. Ohsuna, O. Terasaki, *J. Am. Chem. Soc.* **2000**, *122*, 10712.
[14] a) Y. S. Jung, A. S. Cavanagh, A. C. Dillon, M. D. Groner, S. M. George, S.-H. Lee, *J. Electrochem. Soc.* **2010**, *157*, A75; b) Y. S. Jung, A. S. Cavanagh, L. A. Riley, S.-H. Kang, A. C. Dillon, M. D. Groner, S. M. George, S.-H. Lee, *Adv. Mater.* **2010**, *22*, 2172; c) L. A. Riley, A. S. Cavanagh, S. M. George, Y. S. Jung, Y. Yan, S.-H. Lee, A. C. Dillon, *ChemPhysChem* **2010**, *11*, 2124; d) I. D. Scott, Y. S. Jung, A. S. Cavanagh, Y. Yan, A. C. Dillon, S. M. George, S.-H. Lee, *Nano Lett.* **2011**, *11*, 414.
[15] A. C. Dillon, A. W. Ott, J. D. Way, S. M. George, *Surf. Sci.* **1995**, *322*, 230.
[16] M. A. Montes, D. Suárez, J. A. Menéndez, E. Fuente, *Carbon* **2004**, *42*, 1219.
[17] M. Sevilla, A. B. Fuertes, *Carbon* **2006**, *44*, 468.
[18] A. D. Krawitz, in *Introduction to Diffraction in Materials Science and Engineering* Wiley, New York **2001**, *168*.
[19] S. Laruelle, S. Grugeon, P. Poizot, M. Dollé, L. Dupont, J.-M. Tarascon, *J. Electrochem. Soc.* **2002**, *149*, A727.
[20] V. Chandra, J. Park, Y. Chen, J. W. Lee, I.-C. Hwang, K. S. Kim, *ACS Nano*, **2010**, *4*, 3979.
[21] a) M. D. Groner, F. H. Fabreguette, J. W. Elam, S. M. George, *Chem. Mater.* **2004**, *16*, 639; b) A. W. Ott, J. W. Klaus, J. M. Johnson, S. M. George, *Thin Solid Films* **1997**, *292*, 135.